PAPER • OPEN ACCESS

Density and function of actin-microdomains in healthy and NF1 deficient osteoclasts revealed by the combined use of atomic force and stimulated emission depletion microscopy

IOP ebooks™

Bringing you innovative digital publishing with leading voices to create your essential collection of books in STEM research.

Start exploring the collection - download the first chapter of every title for free.

Density and function of actin-microdomains in healthy and NF1 deficient osteoclasts revealed by the combined use of atomic force and stimulated emission depletion microscopy

Takahiro Deguchi[1,2,9], **Elnaz Fazeli**[2,6,9], **Sami Koho**[2,3],
Paula Pennanen[4], **Maria Alanne**[4], **Mayank Modi**[5,6], **John E Eriksson**[5,6],
Kari V Vienola[2,8], **Pekka E Hänninen**[2], **Juha Peltonen**[4] and
Tuomas Näreoja[2,7,10]

[1] Nanoscopy and NIC@IIT, Italian Institute of Technology, Genova, Italy
[2] Faculty of Medicine, Laboratory of Biophysics, Institute of Biomedicine, University of Turku, Turku, Finland
[3] Molecular Microscopy and Spectroscopy, Italian Institute of Technology, Via Morego 30, 16163 Genova, Italy
[4] Institute of Biomedicine, Cell Biology and Anatomy, University of Turku, Kiinamyllynkatu 10, 20520, Turku, Finland
[5] Faculty of Science and Engineering, Cell Biology, Åbo Akademi University, Turku Finland
[6] Turku Bioscience Centre, University of Turku and Åbo Akademi University, Turku, Finland
[7] Division of Pathology, Department of Laboratory Medicine, Karolinska Institutet, Stockholm, Sweden

E-mail: tuomas.nareoja@ki.se

CrossMark

Abstract

Actin and myosins (IIA, IIB, and X) generate mechanical forces in osteoclasts that drive functions such as migration and membrane trafficking. In neurofibromatosis, these processes are perturbed due to a mutation in neurofibromatosis type 1 (NF1) gene. This mutation leads to generation of hyperactive bone-resorbing osteoclasts that increases incidence of skeletal dysplasia e.g. early-onset osteoporosis in patients suffering from neurofibromatosis. To study the density and function of actin clusters in mutated cells we introduce a new approach for combined use of a stimulated emission depletion (STED) microscope with an atomic force microscope (AFM). We resolved actin-cores within actin-microdomains at four typical structures (podosome-belt, podosome raft, actin patches, and sealing zone) for osteoclasts cultured on bone as well as on glass. Densities of actin-cores in these structures were higher

on bone than on glass, and the nearest neighbor distances were shortest in sealing zones, where also an accumulation of vesicular material was observed at their center. In NF1 deficient osteoclasts, the clustering was tighter and there was also more vesicular material accumulated inside the sealing zone. Using the STED-AFM system, we measured the condensation of the actin structures in real-time after a bone-coated cantilever was placed in contact with a differentiated osteoclast and found that the condensation of actin was initiated at 40 min, after sufficient local actin concentration was reached. A functional implication of the less dense clustering in NF1 deficient cells was that the adhesion of these cells was less specific for bone. The data and new methodologies presented here build a foundation for establishing novel actomyosin dependent mechanisms during osteoclast migration and resorption.

S Supplementary material for this article is available online

(Some figures may appear in colour only in the online journal)

Introduction

There is a wide array of microscopic imaging tools available for preclinical research with specific advantages and constraints. Many of these techniques can be combined or correlated together to gain a better understanding of the specimen. Different forms of super-resolution microscopy have come to age and taken their place in study of molecular mechanisms in cell biology [1, 2]. Atomic force microscopy (AFM) provides unique contrast on specific nano-mechanical properties of different surfaces [3], and serves as a nanomanipulator to induce specific cellular responses. There are many *in vivo* processes that are sensitive to mechanical stimulus, and studying these processes *in vitro* requires precise control of applied forces that is facilitated by the use of AFM. The mechanical forces in cells are often mediated by polymerizing actin, which can conveniently be observed by super-resolution microscopy e.g. stimulated emission depletion (STED) microscopy.

AFM can be used to acquire topographical images of different surfaces, at Ångstrom scale, to probe nano-mechanical properties of living cells [3], and to map interactions with ligands conjugated onto the AFM tip [4]. Using a functionalized tip, AFM images may record transient bio-specific contrast, and without functionalization, provide information on membrane shape and surface elasticity of an object of interest, and cytoskeletal network below it. Thus, the acquired information is complementary to the information provided with optical microscopes, such as specific 3D localization of proteins and other subcellular objects. The diffraction-limited resolution of regular optical microscopes is orders of magnitude inferior to resolution of AFM-data, and therefore, correlative datasets are difficult to interpret.

STED microscopy has made it possible to reach an optical resolution down to a single nanometer in far-field optical microscopy [5, 6]. Furthermore, STED is a point scanning technology that facilitates capturing dynamic events at a small field of view in a live specimen. These properties make STED an attractive option for correlative microscopy applications, as

it works at a similar resolution scale with immunogold electron microscopy and AFM-based techniques. Custom-made and commercial STED microscopes have been coupled with a commercial AFM-systems and used in imaging, nanomanipulation and probing physical properties of a biological sample [7–9]. Correlation between the data from two modalities has typically been achieved after acquisition, based on features observed on both samples or by recording AFM-probe positions [10, 11]. There are three applications for combined STED and AFM: (I) to take images with both STED and AFM for correlative imaging, (II) to combine high-resolution STED images of a region-of-interest with AFM force spectroscopy measurements for ligand interactions and stiffness measurements, and (III) to stimulate living cells by functionalized AFM-probes while taking STED images and recording the responses. We have proposed a simple method to implement correlative imaging (I) on essentially any combination of STED and (tip-scanning) AFM microscopes [11], and now, we present an application where functionalized AFM-probe is used to deliver a biological stimulus (III) and STED microscopy is used to record biological response to the stimulus.

Osteoclasts (OC) are bone-resorbing cells that remove damaged bone and thus play a role in maintaining skeletal health. OCs were induced to differentiate from monocytic precursors by macrophage colony stimulating factor (M-CSF) that upregulates expression of receptor activator of nuclear factor κB (RANK) and by RANK ligand (RANKL) binding to it. Differentiation of mature OCs is initiated by RANKL that upregulates expression of nuclear factor kappa-light-chain-enhancer of activated B cells (NFkB) and nuclear factor of activated T-cells, cytoplasmic 1 (NFATc1), the master regulator of OC-activation. NFATc1 then stimulates its own expression and integrates other converging signals from several costimulatory sources [12, 13], most importantly from the recognition of bone. Osteoclast-associated receptor (OSCAR) [14] is specifically expressed by preOCs and OCs, and it binds to mineralized collagen. Integrin $\alpha_V\beta_3$ recognizes another protein in the bone in an extracellular matrix protein, osteopontin [15,

J. Phys. D: Appl. Phys. **53** (2020) 014003

T Deguchi *et al*

16]. Signals from recognition of these two sources are combined and this leads to an increase in intracellular Ca^{2+} and further activation of NFATc1 [13−15]. NFATc1 then induces differentiation of mature OCs, further enhancing expression of OC-associated genes including *AcP*5 [17] and cathepsin K [18] and stimulating cytoskeletal rearrangement that in turn initiates resorption [15, 16].

OCs contain three types of extracellular matrix-facing actin structures: (i) podosomes (PD), subcellular adhesion sites and mechanosensors [19], typical for glass. On bone are observed (ii) sealing zone (SZ), a functional subcellular structure that attaches the OCs to the bone surface and encircles the area being resorbed [20], and (iii) an actin patch (AP) [21] at ruffled border (RB) has been shown to be the bone dissolving organelle [22] with folded membrane that faces a resorption pit (RP). In many cases, RBs are surrounded by a SZ, but RBs form and function at reduced efficacy even in absence of fully functional SZs [21, 23]. The SZ of osteoclasts cultured on bone is made of interconnected *f*-actin similar to PD-network that excludes vesicular membrane. PDs have been shown to consist of adhesive proteins e.g. integrin $\alpha V\beta 3$ and CD44 clustered around f-actin core along with adaptor proteins like paxillin, cortactin and α-actinin. PDs in healthy OCs cluster together with different degrees of inter-connectivity and are suggested to probe the extracellular milieu. Through this continuous structure, signals reporting on the substrate condition may be transmitted to affect the cell, modulating its responses under physiological and pathological conditions.

Neurofibromatosis type 1 (NF1) is an autosomal dominant genetic disease caused by a germline mutation in the NF1 tumor suppressor gene [24]. This gene encodes protein neurofibromin, which acts as a Ras-GTPase activating protein (RasGAP), and its deficiency leads to hyperactivation of the Ras-pathway [25]. NF1 patients have a lower bone mineral density (BMD) than healthy controls [26] and NF1 is associated with skeletal manifestations such as osteopenia, osteoporosis or debilitating focal skeletal dysplasia [27, 28]. Moreover, hyperactive migration and adhesion have been observed in NF1 preosteoclasts, leading to increased OC-number and bigger OCs with a higher resorption capacity [27–30].

In this study, we observed clustering of actin-cores in different microdomains of an OC and utilize a new approach where bone coated AFM-probe is used to deliver a biological stimulus to induce cytoskeletal rearrangement, while STED microscopy is used to record rearrangement of actin cytoskeleton at the specific subcellular location. Furthermore, we record differences in structures of the actin microdomains and adhesion forces of OCs differentiated from peripheral blood monocytes (PBMCs) of NF1 patients and healthy controls.

Methods

Instrument setup for STED-AFM imaging

Our project started from the idea of combining two arbitrary commercial instruments for STED-AFM correlative imaging—this was to include synchronized instrument control as well as automatic alignment of the multi-modal images

(figure 1). Two commercial microscopes, an Agilent 5500ilm AFM system (Keysight Technologies Inc, USA) and a Leica TCS STED microscope (Leica Microsystems, Germany), were selected for our implementation. To block the STED depletion beam, we placed a long-pass filter (ZIL 0900, Asahi-Spectra USA Inc, USA) in front of the photodiode of the AFM scanner. The selected instruments were initially incompatible and a custom-built stage was constructed to mount the Agilent AFM instrument on our STED system. This made it possible to acquire image data with both modalities simultaneously, as well as to deliver stimuli.

Sample preparations

Two types of OC cultures were utilized: OC cultures were established from human peripheral blood, and from human bone marrow-derived CD34+stem cells (Lonza, Walkersville, USA). Blood-derived human OC cultures ($N = 6$) from peripheral blood were performed as previously described [30, 31]. The blood draw was according to the declaration of Helsinki and approved by the Ethics Committee of Southwest Finland Hospital District with the written informed consents provided from participants. Monocytes were isolated by density gradient centrifugation. Then one million monocytes were seeded on each 12 mm round bone-coated or clean coverslips (#0117520 1.5H precision coverslips Marienfeld, Germany), in 24-well plates and differentiated to multinuclear OCs in alphaMEM (GIBGO, Grand Island, NY, 41061-029) supplemented with 10% iFBS (GIBCO, Grand Island, NY, 16000-044), 1:100 penicillin-streptomycin, RANKL (20 ng ml^{-1}, Peprotech, Rocky Hill, NJ, 310-01) and M-CSF (10 ng ml^{-1}, R&D systems, Minneapolis, MN) for 8–10 d. Half of the medium was changed to fresh one after 3–4 d to preserve auto- and paracrine-signaling molecules. These cells were used for recording force curves, in AFM-stimulated re-organization of the actin cytoskeleton and imaging of actin-microdomains. Overview of the cultures in histological staining identifying OCs is presented in Supplementary figure 1.

Human bone marrow-derived CD34+ stem cells (Lonza) were cultured according to the provider's protocol [32]. The CD34+ stem cells were suspended in culture medium and 100 000 cells were allowed to attach on each 12 mm round bone-coated or clean coverslips in 24-well plates. The culture medium (containing 10% FBS, OCP BulletKit® Lonza,) was supplemented with 33 ng ml^{-1} M-CSF and 66 ng ml^{-1} RANK-ligand (Lonza). After the osteoclast differentiation period on day 7, all culture medium was removed and fresh medium was added into the wells. The mature osteoclasts were cultured for an additional 3 d and fixed for imaging of actin-microdomains.

Staining of fixed samples

Samples were fixed using 4% PFA (ThermoFisher scientific, USA, 28908) for 10 min at room temperature (RT). They were washed 3 times using PBS for 5 min. Furthermore, they were permeabilized and blocked using 0.1% Saponin and 5%
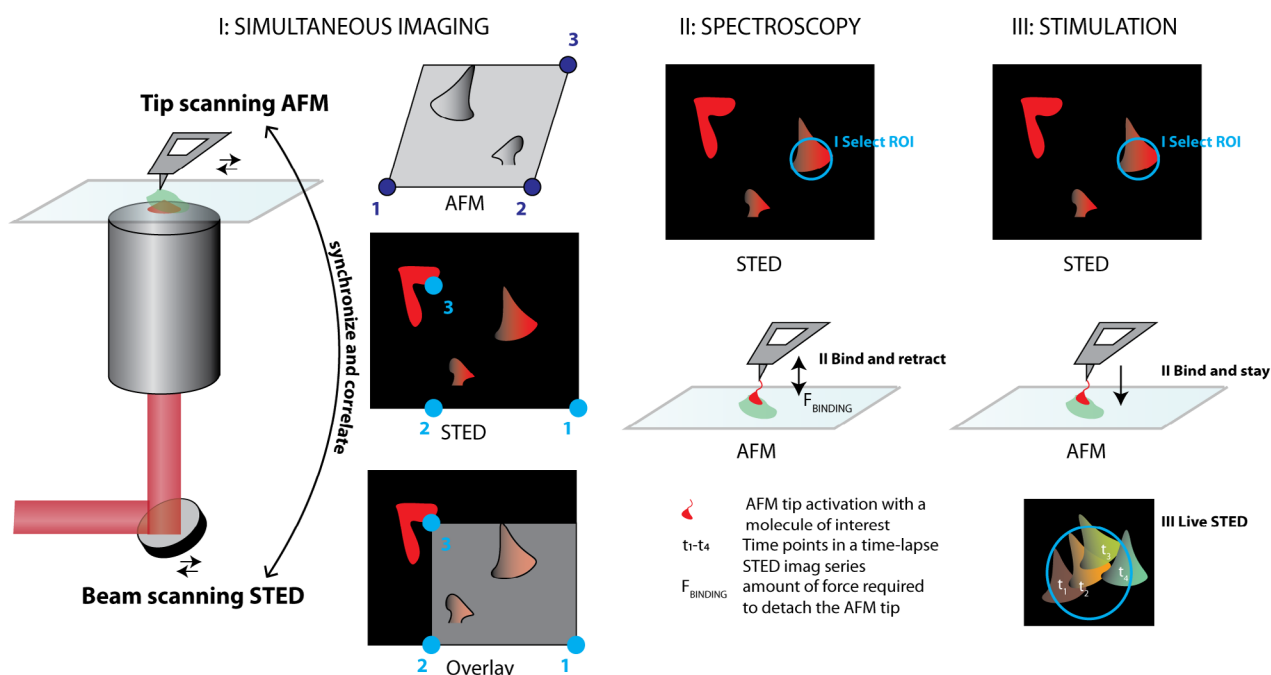
Figure 1. An illustration of three basic types of STED-AFM correlative microscopy applications. In (I) both instruments are used for imaging. The data acquisition in the two instruments needs to be synchronized, and the imaging results need to be registered and overlaid. Our StedAfmCorr software can be used to implement both of these tasks [11]. In (II) super-resolution STED image is used to identify a region-of-interest (ROI) in a live cell sample, to enable targeted AFM force spectroscopy measures. In (III) AFM is used to stimulate responses in a live cell sample, while STED records super-resolution videos of the events that are taking place in the ROI.

normal goat serum (Sigma-Aldrich, USA, S26-100ML) in PBS for 1 h at RT. Next, cells were labeled for actin and membrane using Abberior star 635-phalloidin conjugate (Abberior GmbH, Germany, ST635-0100-20UG) and DiI membrane marker (ThermoFisher scientific, USA, D282), respectively in blocking solution (5% goat serum and 0.1% saponin) and PicoGreen (ThermoFisher scientific, USA, P11496) for 45 min at RT inside humidified chamber. Finally, cells were washed twice using $1\times$ PBS for 5 min and dipped in distilled water and mounted on the slides using Mowiol® mounting media.

Without membrane labeling: Samples were fixed using 4% PFA for 10 min at room temperature. They were washed 3 times using $1\times$ PBS for 5 min and permeabilized using 0.2% triton-X in PBS for 10 min at RT. Consequently, they were washed three times using $1\times$ PBS for 5 min and blocked with 5% normal goat serum for 1 h at room temperature. Next, cells were labeled for actin using Abberior star 635-phalloidin and picogreen for 45 min at RT inside a humidified chamber. Cells were then washed twice using $1\times$ PBS for 5 min and dipped in distilled water and mounted on the slides using Mowiol® mounting media.

Fluorescence imaging of fixed specimens

We used two instruments to acquire confocal and STED microscopy images, Leica SP5 STED microscope (Leica microsystems GmbH, Germany) equipped with a Ti:sapphire depletion laser and Abberior Instruments Expert Line STED system (Abberior Instruments GmbH, Germany) equipped with 775 nm laser. With the Leica system, the fluorescent dye Atto647N was excited with a pulsed 635 nm laser and depleted

at 770 nm in case of live OCs and at 750 nm in case of fixed samples. The fluorescence signal was detected by an avalanche photodiode (APD) detector with a band-pass fluorescence filter of 665–705 nm range. For the live OC imaging, the same settings were used for imaging but without the depletion laser. With the Abberior system, Abberior STAR 635-phalloidin was excited with a pulsed 635 nm laser and depleted at 775 nm using a continuous-wave depletion laser with a time-gating detection of 1.7 to 2 ns temporal window. Confocal images of the membrane were taken using 561 nm laser and emission signal was detected using 615(20) APD.

Live confocal/STED imaging upon AFM stimulation of OC

For live STED-AFM imaging, cells were stained for *f*-actin using phalloidin-Atto647N (ATTO-TEC GmbH, Germany) with 200 ng ml^{-1} concentration and 30 min of incubation time in the cell culture medium. After staining the medium was changed to fresh medium and the cells were allowed to recover for 1 h prior to imaging. The 12 mm round coverslip with OC on top was placed in an AFM sample holder and cells were kept in the culture medium described above. The microscope was equipped with an environment chamber for live-cell imaging and thus the cells inside the chamber were kept at 37 °C and 5% CO_2.

Using a bright-field microscope, we selected a mature osteoclast, which had more than 3 nuclei (Supplementary figure 1), and placed the bone coated cantilever on top of the cell with a deflection of 1 V. Then fluorescence imaging of *f*-actin channel was started with the configurations and parameters described above using the Leica STED microscope. After

J. Phys. D: Appl. Phys. **53** (2020) 014003

T Deguchi *et al*

taking confocal images at three different z-positions (0, 4, and 7 μm), live confocal imaging was started at the z-position of 7 μm, at which the cell-bone interface was visible. The confocal image was taken every 15 s for 40 min. After this confocal time-lapse imaging, two live STED images were taken with 10 min interval at the same z-position.

Image processing and analysis

The STED images were deconvolved using blind iterative Richardson Lucy algorithm that was recently proposed in [33]. The deconvolution, with background correction enabled, was run for only five iterations, mainly to eliminate the strong background noise that would have otherwise interfered with the image segmentation.

For the nearest neighbor distance (NND) analysis of f-actin structures, we used the following protocol using functions and plugins in Fiji (ImageJ version 1.52n). First, images were smoothed using Gaussian blur with a sigma value of 1.5 pixels. The images were further processed using FeatureJ plugin using the Laplacian algorithm with a smoothing factor of 3.0 (or 7.5 in case of confocal images), followed by an automatic Otsu threshold and watershed. Thereby generated binary images were analyzed for the centroid coordinates within ROI-areas encompassing the actin-microdomain using Analyze Particles function with a size of 0.01—infinity μm^2 (0.09—infinity μm^2 in case of confocal) and circularity of 0.0–1.0. Comparison of NNDs for the PD-belt, PD-raft, SZ, AP was performed by analyzing seven independent images each containing more than 100 centroids for the structures, respectively. Finally, the Euclidian distances from each of the centroids to the 10 nearest neighboring centroids were calculated.

Bone functionalized AFM cantilever

To activate an osteoclast for bone resorption, a tip-less AFM cantilever (CSC12, CSC12/tipless/no Al, MikroMasch®, Innovative Solutions Bulgaria Ltd., Sofia, Bulgaria) coated with bone nanoparticles. For this purpose, expired biobanked human bone was used [21]. The cantilever was coated with bone using a previously described method [21]. Briefly, the surface of a tip-less cantilever was chemically functionalized using APTES ((3-aminopropyl)triethoxysilane)/ethanolamine) coating and nanometer size human bone particles or 0.1% BSA were deposited on the cantilever in a phosphate coating buffer. After overnight incubation, the cantilever was fixed with 4% paraformaldehyde for 30 min and washed gently with PBS.

### *Instrument setup for force spectroscopy*

The measurement of the OC adhesion force to the bone coated AFM cantilever was carried out with a protocol used in the previous study [21]. Briefly, the adhesion force was measured using an AFM equipped with a CellHesion module (JPK Instruments, Berlin, Germany) on a Zeiss LSM 510 confocal microscope (Carl Zeiss). During the experiment, cells were kept in alphaMEM (GIBGO, Grand Island, NY, 41061-029) supplemented with 10% iFBS (GIBCO, Grand Island, NY, 16000-044), 10 mM HEPES (Sigma-Aldrich, H0887), 1:100 penicillin-streptomycin. Upon the measurement, first the bone coated cantilever was placed on OCs with 4–6 nuclei at the cantilever deflection of 2 V. Next, the cantilever was kept on the OCs at three different extraction delay times, 30, 120, and 300 s. Then, as the third step, the cantilever was retracted from the OCs. During these processes, the force applied at the cantilever over the distance of 70–100 μm was recorded as force curves. Recorded force-distance curves were analyzed to calculate adhesion energy, area separating retraction-curve (dark red) and the approach-curve (bright red), by JPK Data Processing software (JPK Instruments). The measurement was repeated on each cell at least ten times. The cells were kept at 37 °C during the entire measurements. For statistical evaluation Mann–Whitney test was conducted for each of the four combinations of OCs and coated cantilevers with the following sample numbers: $N = 5$ samples of healthy OCs and BSA coated cantilevers, $N = 6$ samples of healthy OCs and bone-coated cantilevers, $N = 4$ samples of NF1 OCs and BSA coated cantilevers and finally $N = 5$ samples of NF1 OCs and bone-coated cantilevers.

## Results

Actin patterns are substrate specific

We investigated organization of actin structures and patterning of actin-cores in relation to substrate by culturing OCs on glass and bone and imaged actin structures with super-resolution STED microscopy. We measured distances between PDs and actin-cores in SZs and APs to gain insight into generation of mechanical forces deforming OCs' plasma membrane. On glass PD-rings (figures 2(A)–(C)) and PD rafts (figures 2(D)–(F)) were observed. PD rafts were present in different shapes and sizes and typically consisted of more than 50 PDs. The PD rings were typically present at the circumference of OCs and consisted of more than 100 PDs distributed in a 1–5 PDs wide line. On bone, OCs formed different types of actin-microdomains, SZs and APs, associated with RBs. The SZs were also ring-like entities (figures 2(G)–(I)) and could be resolved to consist of closely packed f-actin puncta instead of a uniform band of f-actin. The shape of actin puncta in APs was similar to SZs (figures 2(J)–(L)), although more variation could be seen. The APs have been shown to include many of the adaptor-proteins found in other actin-microdomains. We went on to describe the density of actin puncta in these microdomains by NND analysis (figure 2(M)). In the NND analysis, actin structures were segmented into small pieces and the distances from each centroid of the segments to the nearest segments (from 1st up to 10th nearest neighboring centroids) were compared. The NNDs were longer for PD-belt and raft than for AP and SZ, and the SZ presented the shortest NNDs (figure 2(M)). The distances of PDs in rafts and belts were comparable, however, the variation
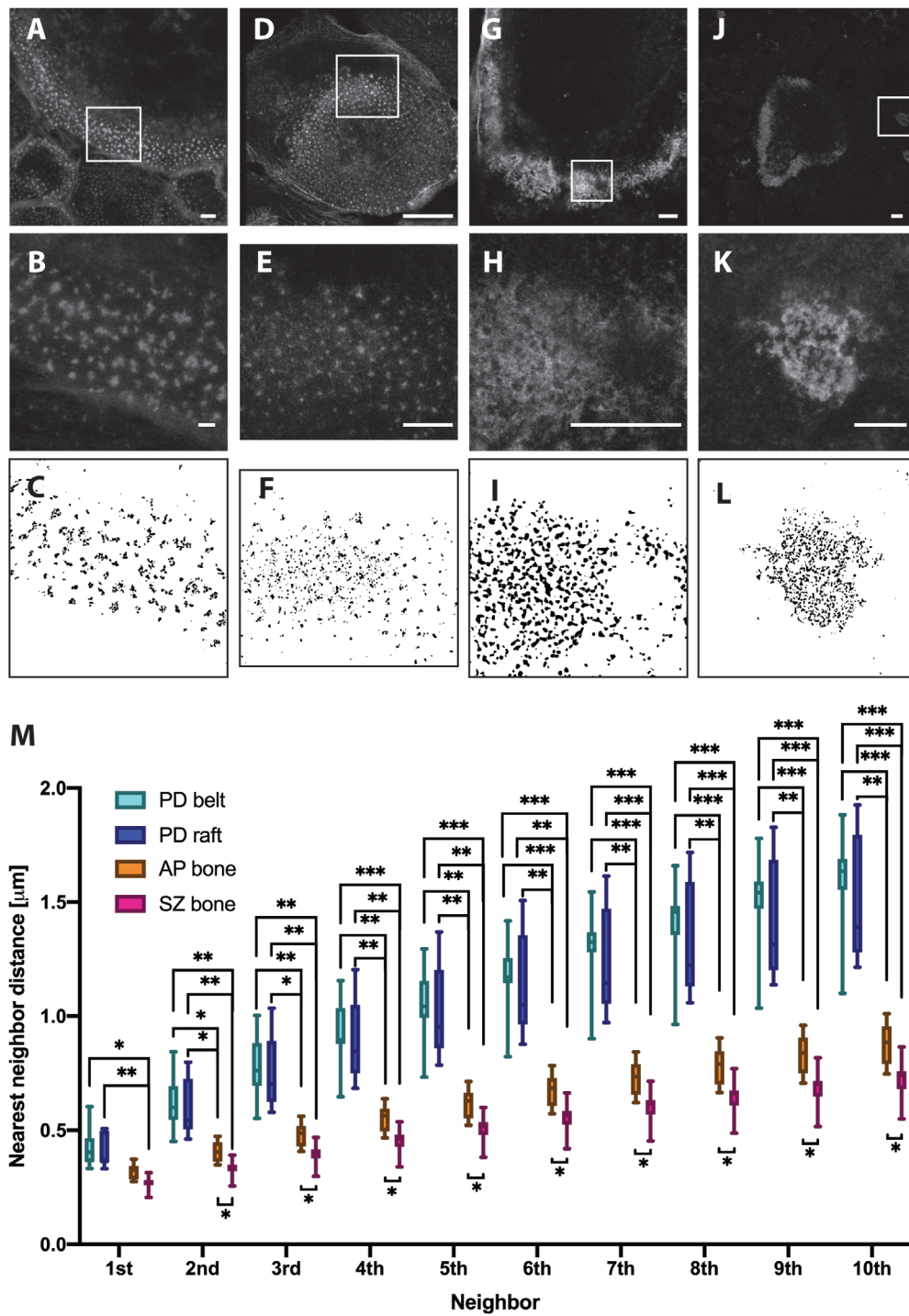
Figure 2. Actin-microdomains in healthy OCs adopt substrate-specific organizations. STED micrographs of phalloidin stained f-actin in (A) and (B) PD-belt. (C) Thresholded binary image identifying the actin-cores. Images show actin cores in (D)–(F) PD-raft, (G)–(I) from SZ and (J)–(L) from AP. Scalebar in all images 5 μm. (M) NNDs of the actin cores within each of actin-microdomains from 1st (closest) to 10th neighbor in μm. The observations were tested to be normally distributed with the Shapiro–Wilk test and differences between were tested with two-way ANOVA. $^*p < 0.05$ $^{**}p < 0.01$ $^{***}p < 0.001$. (A), (B), (D) and (E) are taken using the Abberior STED system, and (G), (H), (J) and (K) are taken using the Leica SP5 system.

in distances in PD rafts was higher. This could imply a higher level of organization in PD belts. Slightly shorter NNDs were measured in rafts, most likely due to the wider shape of the structure. The NNDs in structures on bone (AP, SZ) were significantly shorter than on glass (PD belt and raft), indicating that substrate recognition drives this process, possibly

due to an abundance of epitopes for adhesion proteins present on bone. Contrary to the PD structures, between SZ and AP there was a difference in NNDs from the 2nd neighbor and longer. The NNDs in SZ were shorter and variation in the distances was also the lowest among the microdomains measured.
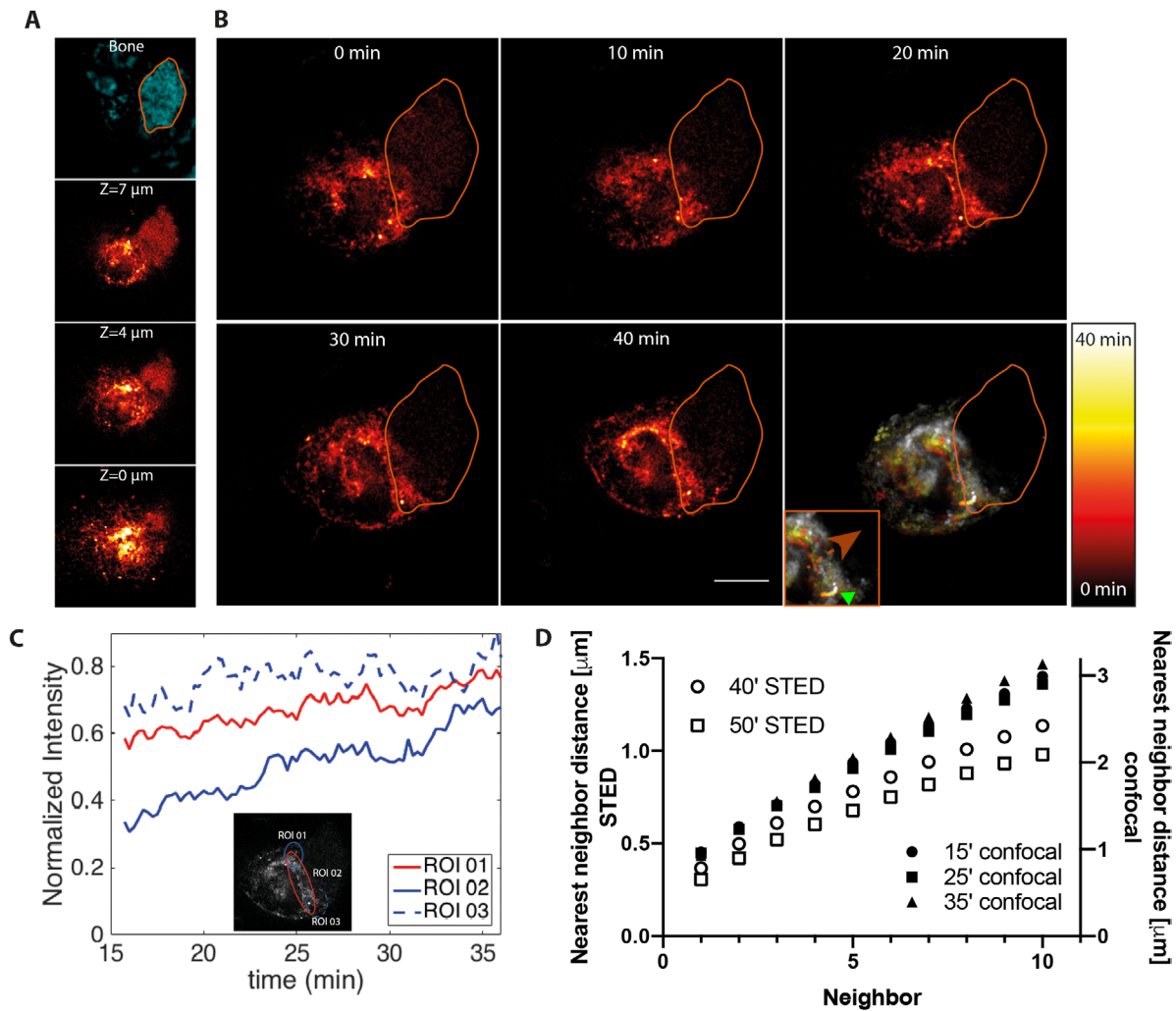
Figure 3. Actin reorganization upon bone contact. The figure presents a representative f-actin structure in OC taken by time-lapse confocal microscopy. (A) Actin morphologies of an OC shown at three different *z*-positions (0, 4, and 7 μm) and the reflection showing bone at the *z*-position of 7 μm at the basolateral membrane of the cell. (B) Actin morphological changes with 10 min interval for over 40 min at the cell-bone interface (Annotation representing bone border). The temporal-color coded image of the time-lapse shows that brighter color representing later time points are found closer to the bone border. The inset shows a closer view, showing actin accumulation at the cell-bone interface. (C) Intensity increase over time in three ROIs, shown in the inset image, at the cell-bone interface. All the ROIs showed intensity increase, presenting the actin accumulation at the cell-bone interface. (D) Condensation of NNDs actin-cores during the time-lapse series. NNDs of the actin cores within the stimulated section from 1st to 10th neighbor in μm, at a given time point, were plotted. Observations at 15–35 min are done with confocal 15$'$ (●), 25$'$ (■) and 35$'$ (▲). NNDs remain unchanged until 35 min when a small increase in NNDs is measured. Subsequent time-points 40$'$ (○) and 50$'$ (□) are captured with STED resolution. At 50 min the NNDs are closer to NNDs typically observed on bone than ones observed on the glass.

Dynamic clustering of PDs is initiated by substrate recognition

It has been shown that both PDs and SZs dynamically form, reshape, deform and disappear. We wanted to estimate the directionality of the clustering when cells come to contact with bone. The process was induced by placing a bone coated AFM cantilever on top of a multinuclear OC cultured on glass, while observing changes in *f*-actin structures (figure 3). At the beginning of the experiment we recorded *f*-actin structures on coverslip 0 μm, half-cell height 4 μm and at cantilever interface 7 μm (figure 3(A)). *F*-actin intensity was mainly accumulated on the coverslip plane in adhesion structures. The cantilever was placed in contact to the OC on a side without any apparent adhesion structures, and an actin accumulation

was first observed without STED but only with confocal due to phototoxicity concerns (figure 3(B)). A time-lapse image series in the f-actin channel was captured for 40 min with an interval of 15 s at the *z*-position of 7 μm above the coverslip in order to track the actin morphological changes at the cell-bone interface. Accumulation began after 10 min (figure 3(B)) and had reached a maximum at 30 min at most parts of the cantilever (figure 3(C)). To understand the significance of this phenomenon, we observed also a condensation of the actin structures in NNDs. Despite of actin accumulation, the NNDs remained unchanged for 30 min and at 35 min we noticed a slight increase (figure 3(D)). The increase is likely due to insufficient resolution of the confocal microscope as the actin structures are recorded as a single entity, and therefore, we started to capture STED frames. In the STED frames, we

J. Phys. D: Appl. Phys. **53** (2020) 014003

T Deguchi *et al*
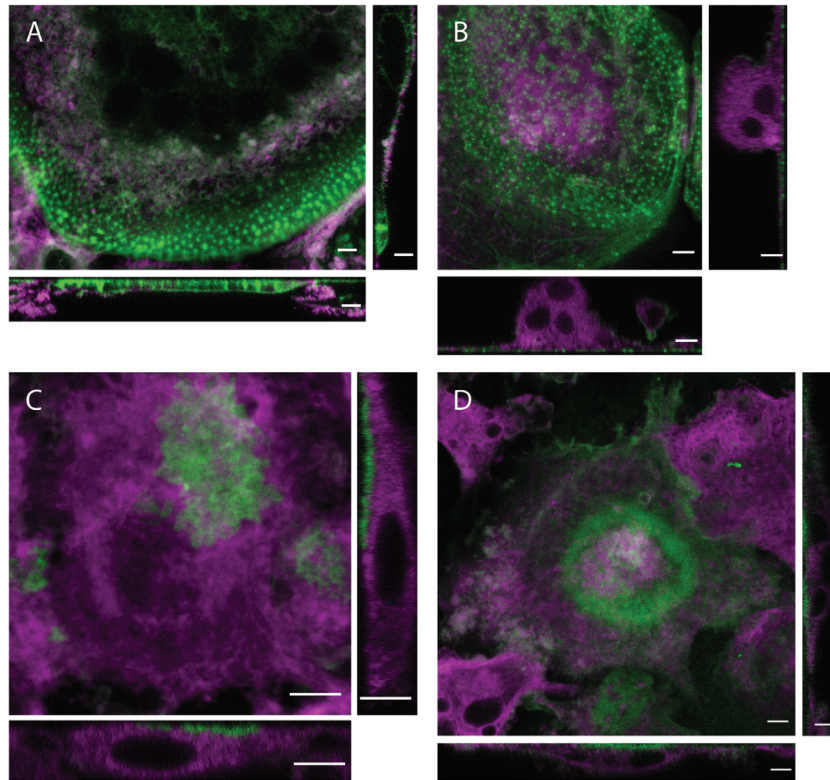
Figure 4. Membrane structures accumulate inside SZ, while they distribute evenly in the cytoplasm with the other actin-microdomains. (A) Sum-intensity and orthogonal view of PD-belt in PBMC derived OCs. Actin (green) labeled with phalloidin and DiI membrane marker (magenta) taken with Leica SP5. (B) Sum-intensity and orthogonal view of PD-raft in PBMC derived OCs. (C) Sum-intensity and orthogonal view of AP in bone marrow macrophage derived OCs. (D) Sum-intensity and orthogonal view of SZ in bone marrow macrophage-derived OCs. Horizontal orthogonal view showing *XZ* and vertical showing *YZ* directions. Scalebar in sum intensity images and *XZ* images are 5 μm and for *YZ* images is 3 μm.

observed a condensing trend within 10 min interval (figure 3(D)). Comparing NNDs of f-actin clusters to the cells cultured on bone and glass, at 50 min stimulation, the NNDs in the bone-cantilever stimulated cell were closer to the NNDs observed on AP and SZ than in PD structures (figures 2(M) and 3(D)). Observing the clustering process in real-time, we recorded PDs form and dissipate, but also, some *f*-actin clusters that remained stable and migrated over time (figure 3(B) green arrowhead). The temporal color-coded image of the time-lapse data presents the trace of the movement (figure 3(B)). This would indicate condensation of preexisting actin clusters, possibly induced by forces generated through actin polymerization or by non-muscle myosins. Such a process could mediate changes in membrane tension, and in part, facilitate membrane trafficking and generation of protrusions at RB.

F-actin clustering at SZ facilitates accumulation of membrane at RB

To test if membrane trafficking is modulated by the different actin-microdomains, we stained membrane compartments with a lipophilic dye DiI. DiI binds initially to the plasma membrane, and subsequently as a result of membrane recycling, spreads to most other membrane compartments within a cell. Examining the PD-structures (figures 4(A) and (B)) we detected a low intensity of membrane staining on top of the actin structures, and ER and vesicular membrane distributed diffusely throughout the cytoplasm. In the case of OCs cultured on bone, at AP a similar trend was observed or a slight accumulation of intensity above the structure was found (figure 4(C)). In SZ (figure 4(D)), we observed an area nearly devoid of membrane staining directly above the structure and an accumulation of membrane at its center. The accumulation is illustrated in an orthogonal section and a sum-intensity projection (figure 4(D)). This result is consistent with prior electron microscopy data illustrating a high amount of diverse membrane structures [34]. This observation indicates an association between the clustering of actin-microdomains and membrane trafficking. The functional implication of the association could be the regulation of membrane tension that in turn would provide the necessary forces to mediate vesicle fusion at RB.

Actin in APs of NF1 $\pm$ OCs is less condensed and SZs contain more membranous compartments within

The morphology of the NF1 cells appeared similar to healthy controls, although OCs were larger and contained more nuclei (figure 5). According to previous reports, actin dynamics in NF1 OCs is perturbed and this has been predicted to be the underlying factor in increased resorption. Appearances of the actin-microdomains, PD-rafts, PD-belts, and SZs, seemed similar to the healthy controls (figures 5(A)–(D)), while the
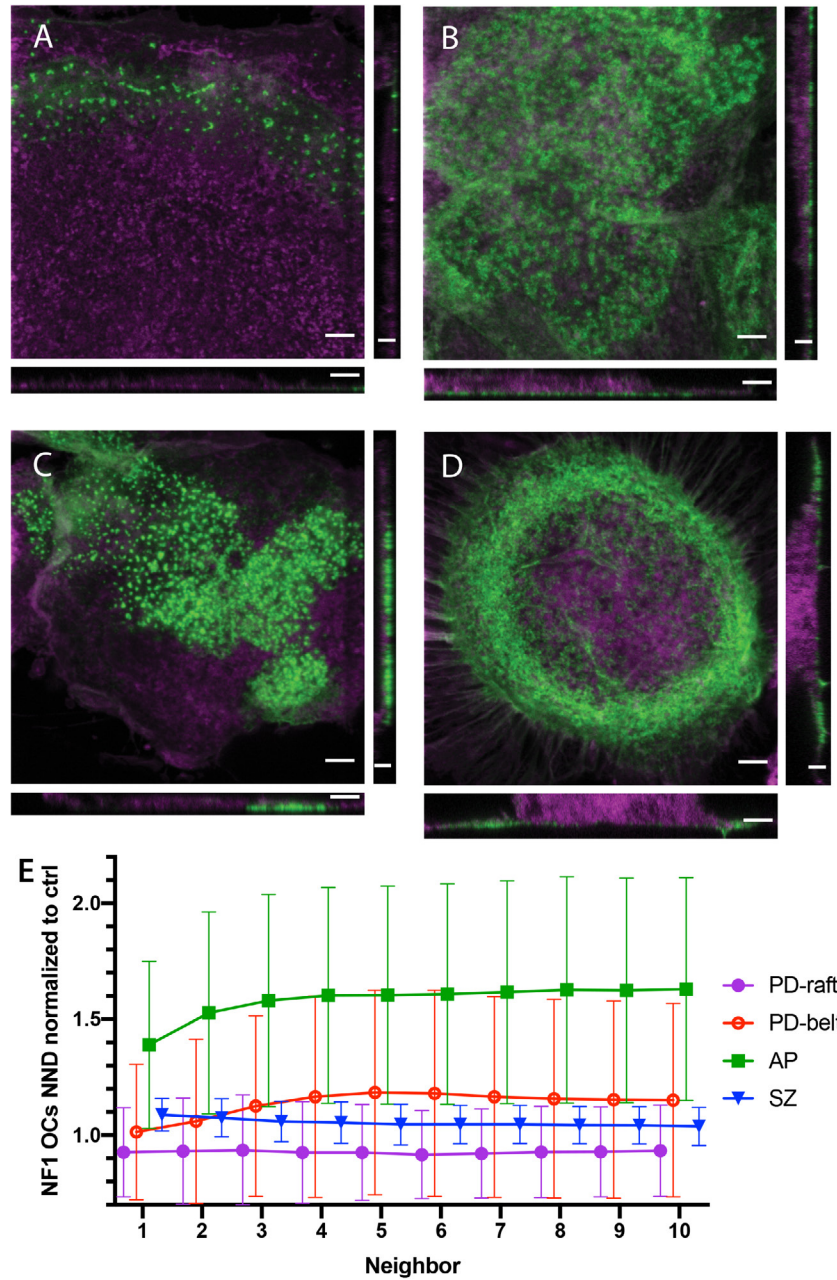
Figure 5. Actin and membrane structures appear similar in NF1 OCs, but discrepancies in NNDs are observed. (A) Sum-intensity and orthogonal view of PD-belt in NF1 $\pm$ PBMC derived OCs. Actin (green) labeled with phalloidin and DiI membrane marker (magenta) taken with the Abberior STED. (B) Sum-intensity and orthogonal view of PD-raft. (C) Sum-intensity and orthogonal view of AP. (D) Sum-intensity and orthogonal view of SZ. Horizontal orthogonal view showing *XZ* and vertical showing *YZ* directions. Scalebar in sum intensity images and *XZ* images are 5 μm and for *YZ* images is 3 μm. (E) Ratios of NNDs within each of actin-microdomains in NF1 OCs compared to NNDs of actin-microdomains in healthy controls (shown in figure 2). The NNDs in APs are approximately 50% longer in NF1 OCs than in healthy controls.

APs in NF1 OCs resembled more PDs than APs in healthy controls (figure 5(C0). To examine this hypothesis in more detail we compared the NNDs of actin-microdomains in NF1 OCs with the healthy counterparts on both, glass and bone (figure 5(E)). Especially APs appeared to be less dense than in healthy counterparts (figures 5(C) and (E)). Also, quite surprisingly, NNDs in PD-rafts were shorter in NF1 OCs, while NNDs in PD-belts were longer, indicating that the PD-domains might be functionally dissimilar. In NF1 OCs, the NNDs at SZs were only slightly longer, nevertheless, we measured higher intensity of membrane staining within the SZs compared to healthy controls. It would appear that these observations could reflect the higher resorption capacity of NF1 OCs. While the resorption capacity itself cannot be taken to represent a risk for osteoporosis, a failure in regulation of resorption could constitute such a risk.

J. Phys. D: Appl. Phys. **53** (2020) 014003

T Deguchi *et al*

Adhesion of NF1 ± OCs is less specific suggesting impaired recognition of sites for resorption

To examine the functional implications of the differences in NNDs and to understand what causes the reported higher rate of resorption, adhesion forces between OCs and substrate were measured. Cantilevers coated either with BSA (figure 6(A)) or bone particles were placed on multinuclear cells and adhesion forces were recorded after 30 s, 120 s, and 300 s. The maximum adhesion force between OCs from healthy donors and bone-coated cantilevers was around 100 nN while this value between NF1 OCs and bone-coated cantilevers was around 250 nN (figures 6(B)–(C)). Maximum adhesion force value was also measured between OCs and BSA coated cantilevers and it showed less adhesion, around 30 nN between healthy OCs and BSA cantilevers and 80 nN for NF1 OCs.

Adhesion energy is a more accurate representation of adhesion compared adhesion force, because it considers all unbinding events as an integral. In this regard, the NF1 OCs had higher adhesion energy than healthy OCs towards both BSA and bone (figure 6(D)). This difference between NF1 and healthy, however, was not significant. More importantly, the NF1 OCs did not have a significant difference in adhesion energy between bone and BSA (figure 6(D)). The differences of adhesion energies between healthy OCs and bone-coated cantilevers at 120 and 300 s contact time points were significantly different from adhesion to BSA coated cantilevers (figure 6(D)).

Discussion

Considerable effort has been placed in studying actin dynamics in OCs. Previous studies [35–38] have demonstrated the cyclic nature of actin-microdomains in OCs. Dynamics of PD movement have been described as directed flow patterns of f-actin, vinculin, and talin coordinated between neighboring PDs [39]. The observation of SZs forming and expanding before dissipating [40] resembles the observations in dendritic cells. With super-resolution microscopy, we observed that a SZ on bone consists of subunits similar to the PDs observed on the glass. The distances between these subunits, however, were shorter than the distances between PDs. On glass, we did not observe any difference in NNDs between PD-rings and PD-rafts in healthy OCs. On bone, the actin structures were denser than on glass and NNDs in SZs were shorter than in APs. Live imaging studies have shown that SZs form from APs [37, 41], and this indicates that there must be a condensation phase before AP transforms into SZ. Moreover, once condensed the SZ appears to move as a single entity, maintaining its organization although its position and shape changes, sometimes over extended periods of time [41]. The stability of SZs could be an inherent property of an OC or be induced by properties, e.g. abundance of exposed extracellular matrix proteins on the substrate. PDs, however, can move together, and they also appear and disappear while migrating [39].

When a bone-coated cantilever was placed on an OC, f-actin accumulated at the interface and clustered tighter after 30 min time of the initial contact. Within the 30 min active signaling can be involved in the clustering-process, and possibly, initial effects of transcriptional changes induced by the already primed OSCAR—NFATc1—pathway [15] are seen. During the time-lapse imaging f-actin structures in the bone-stimulated OC, cultured on the glass, had adopted NNDs comparable to the values in APs and SZs measured in cells cultured on bone. We observed an accumulation of membrane structures within SZs, implying very low membrane tension [42]. Similar membrane accumulation was not observed above nor in the proximity of the other studied actin structures. This membranous material represents acidified vesicles ready for exocytosis, endocytosed vesicles with resorption products, protrusions, and ruffles. The condensation from AP to SZ could be a possible mechanism to initially reduce the membrane tension.

After SZ forms in a second phase, it predominantly expands while it moves during resorption [40, 37]. Our results indicate actin-clustering as a mechanism that could provide necessary attenuation of membrane tension to and forces to mediate vesicle fusion at RB. Outward expansion of SZ is likely to reduce membrane tension by pulling membrane to the baso-lateral sides facilitating the collapse of acidified vesicles at the plasma membrane RB and thereby exocytosis of acidified vesicles [42]. Furthermore, inhibition of myosin II was shown to reduce cell stiffness [43], reduce PD migration in dendritic cells [19] and drive vesicle exocytosis [44], an effect which was comparable to latrunculin A treatment of the cells [45]. These studies, combined with our observations, indicate a role for actomyosin-complex [46] in mediating forces required for both re-patterning actin-microdomains and for forming and expanding SZs. Myosin IIA has been shown to generate protrusion forces at PDs [19], and therefore, the clustering of actin cores may be directly achieved by myosin IIA contraction between PDs [46], similar to exocytosis of large secretory granules [45]. The SZ and PDs both contain largely the same adaptor protein interacting with f-actin network [47, 48]. The formation and expansion of SZs were shown to be attenuated by knockdown and overexpression of myosin X, which was localized at the outer edge of SZ and PD rings [23]. Actomyosin interactions have been shown to be regulated by ADF/cofilin [49] through competitive interactions [50] and the same mechanism has been studied in PD-belt formation [51].

Signaling leading to ADF/cofilin (cofilin) has been shown to proceed via the Rho-ROCK-LIMK-2(LIM kinase-2)-cofilin pathway that is disrupted in NF1 deficient cells [52, 53]. Actin dependent functions e.g. migration have been reduced upon NF1 knockdown as accumulating phospho-cofilin is able to sever actin filaments. Therefore, we examined properties of the actin-microdomains in NF1 ± OCs. We observed disrupted f-actin clustering of the OCs as shown by the NNDs normalized against healthy controls as predominantly longer NNDs. In NF1 OCs PD-rafts were denser throughout the structure, while in PD-belt actin-cores had longer distances to adjacent PDs. This may have been caused by the accumulation of phospho-cofilin and severing of the actin filaments connecting PDs, but also, by cofilin binding to actin filaments that is able

J. Phys. D: Appl. Phys. **53** (2020) 014003

T Deguchi *et al*
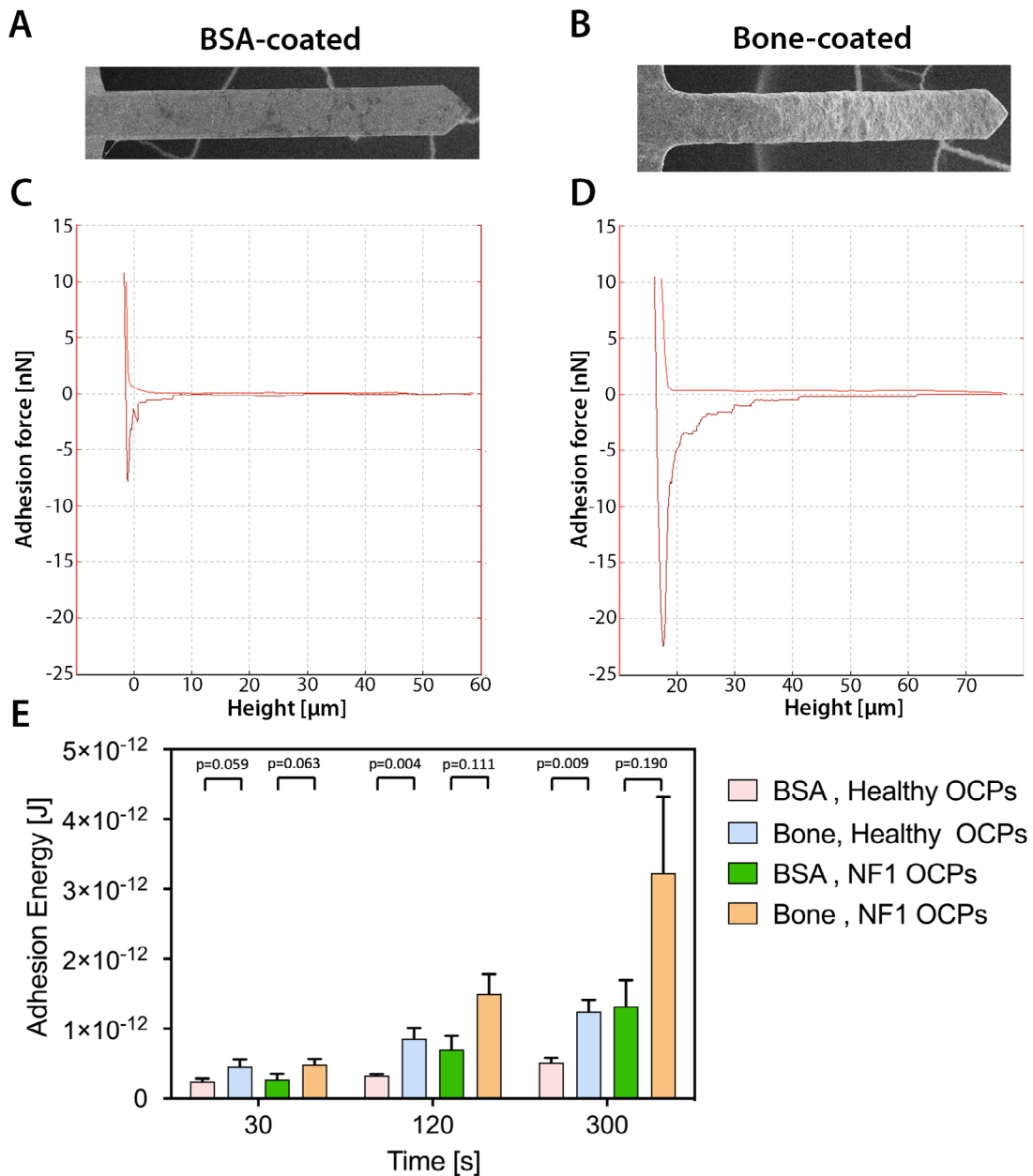
Figure 6. Adhesion forces of NF1 deficient and healthy OCs on coated cantilevers. (A) Scanning EM image of a BSA-coated cantilever and (B) a bone-coated cantilever. Examples of force curves of adhesion onto bone-coated cantilever of a (C) healthy OC and (D) NF1 OC. Recorded force-distance curves were analyzed to calculate adhesion energy, area separating retraction-curve (dark red) and the approach-curve (bright red). Comparison of statistical analysis between (means ± standard errors and Mann–Whitney *p*-values) of different groups (E) Healthy OC adhesion to bone versus BSA coated cantilevers, as well as NF1 OC adhesion to bone versus BSA coated cantilevers. $N = 5$ with healthy OC versus BSA, $N = 6$ with healthy OC versus Bone-coated cantilevers, and $N = 4$ with NF1 OC versus BSA, $N = 5$ with NF1 OC versus Bone-coated cantilevers assessed for three contact time points: 30 s, 120 s and 300 s in GraphPad Prism.

to outcompete myosin II binding preventing further condensation of the f-actin connecting the PDs. PD-rafts are more dynamic than PD-belts, and hence, more susceptible to cofilin hyperactivity, also this would be consistent with observations of reduced migration. Similar findings on bone in APs of NF1 OCs the NNDs were much longer than in healthy controls. The active phospho-cofilin is able to sever *f*-actin filaments, and thereby, prevent formation of force-mediating actomyosin complexes. As APs are perceived to be a preliminary phase

for SZs, and therefore, their emergence would require a signal from the extracellular matrix to begin resorption. In this context, fewer forming SZs might also make the existing SZs more stable, less migratory and dynamic in outward expansion and more persistent. These outcomes would agree well with previous results [30] and build a hypothesis that resorption is less precisely regulated in NF1 OCs.

We examined the functional outcomes of the Ras-hyperactivity [25] and found that adhesion was affected in

J. Phys. D: Appl. Phys. **53** (2020) 014003

T Deguchi *et al*

the NF1 OCs. There was a trend of higher adhesion forces in the NF1 OCs, but these were not significantly different from the healthy controls. However, in healthy OCs adhesion to bone was significantly stronger than to BSA, while in NF1 OCs such difference was not present. This loss of specificity implies that regulation of resorption has been lost to some extent while resorptive capacity has increased [30]. The loss of regulation may explain also other skeletal dysplasia associated with neurofibromatosis [28].

Conclusions

In summary, we have characterized the density of actin-cores in OC specific f-actin microdomains by using STED-microscopy. With novel methodology combining STED and AFM, we have demonstrated the timescale of the substrate-specific signaling through which OCs adapt to and polarize towards bone, and also, we suggest a potential mechanism for exocytosis of acidified vesicles through membrane tension that in turn is modulated by actomyosin complexes. Furthermore, we showed discrepancies in actin structures of NF1 OCs that follow hyperphosphorylation of cofilin.

Acknowledgements

Disclosures

The authors declare that they do not have any conflicting financial interests.

ORCID iDs

Takahiro Deguchi https://orcid.org/0000-0002-3195-1488
Elnaz Fazeli https://orcid.org/0000-0002-0770-0777
Sami Koho https://orcid.org/0000-0003-3927-1687
Kari V Vienola https://orcid.org/0000-0003-3390-392X
Juha Peltonen https://orcid.org/0000-0002-5732-4167
Tuomas Näreoja https://orcid.org/0000-0002-2174-4434

References

[1] Moerner W E 2012 Microscopy beyond the diffraction limit using actively controlled single molecules *J. Microsc.* **246** 213–20
[2] Vangindertael J *et al* 2018 An introduction to optical super-resolution microscopy for the adventurous biologist *Methods Appl. Fluoresc.* **6** 022003
[3] Raman A *et al* 2011 Mapping nanomechanical properties of live cells using multi-harmonic atomic force microscopy *Nat. Nanotechnol.* **6** 809–14
[4] Girish C M *et al* 2009 Atomic force microscopic study of folate receptors in live cells with functionalized tips *Appl. Phys. Lett.* **95** 223703
[5] Wildanger D *et al* 2012 Solid immersion facilitates fluorescence microscopy with nanometer resolution and sub-ångström emitter localization *Adv. Mater.* **24** OP309–13
[6] Vicidomini G, Bianchini P and Diaspro A 2018 STED super-resolved microscopy *Nat. Methods* **15** 173–82
[7] Harke B, Chacko J V, Haschke H, Canale C and Diaspro A 2012 A novel nanoscopic tool by combining AFM with STED microscopy *Opt. Nanoscopy* **1** 3
[8] Chacko J V, Canale C, Harke B and Diaspro A 2013 Sub-diffraction nano manipulation using STED AFM *PLoS One* **8** e66608
[9] Chacko J V, Zanacchi F C and Diaspro A 2013 Probing cytoskeletal structures by coupling optical superresolution and AFM techniques for a correlative approach *Cytoskeleton* **70** 729–40
[10] Monserrate A, Casado S and Flors C 2014 Correlative atomic force microscopy and localization-based super-resolution microscopy: revealing labelling and image reconstruction artefacts *ChemPhysChem* **15** 647–50
[11] Koho S, Deguchi T, Löhmus M, Näreoja T and Hänninen P E 2015 A software tool for STED-AFM correlative super-resolution microscopy *Proc. SPIE* **9330** 93301K–7
[12] Kim J H and Kim N 2016 Signaling pathways in osteoclast differentiation *Chonnam Med. J.* **52** 12–7
[13] Kim J H and Kim N 2014 Regulation of NFATc1 in osteoclast differentiation *J. Bone Metab.* **21** 233–41
[14] Kim Y *et al* 2005 Contribution of nuclear factor of activated t cells c1 to the transcriptional control of immunoreceptor osteoclast-associated receptor but not triggering receptor expressed by myeloid cells-2 during osteoclastogenesis *J. Biol. Chem.* **280** 32905–13
[15] Park J H, Lee N K and Lee S Y 2017 Current understanding of RANK signaling in osteoclast differentiation and maturation *Mol. Cells* **40** 706–13
[16] Chambers T J and Fuller K 2011 How are osteoclasts induced to resorb bone? *Ann. New York Acad. Sci.* **1240** 1–6
[17] Takayanagi H *et al* 2002 Induction and activation of the transcription factor NFATc1 (NFAT2) integrate RANKL signaling in terminal differentiation of osteoclasts *Dev. Cell* **3** 889–901
[18] Matsumoto M *et al* 2004 Essential role of p38 mitogen-activated protein kinase in cathepsin K gene expression during osteoclastogenesis through association of NFATc1 and PU.1 *J. Biol. Chem.* **279** 45969–79
[19] Labernadie A *et al* 2014 Protrusion force microscopy reveals oscillatory force generation and mechanosensing activity of human macrophage podosomes *Nat. Commun.* **5** 5343
[20] Takito J, Inoue S and Nakamura M 2018 The sealing zone in osteoclasts: a self-organized structure on the bone *Int. J. Mol. Sci.* **19** E9840
[21] Deguchi T *et al* 2016 *In vitro* model of bone to facilitate measurement of adhesion forces and super-resolution imaging of osteoclasts *Sci. Rep.* **6** 22585
[22] Stenbeck G 2002 Formation and function of the ruffled border in osteoclasts *Semin. Cell Dev. Biol.* **13** 285–92
[23] McMichael B K, Cheney R E and Lee B S 2010 Myosin X regulates sealing zone patterning in osteoclasts through linkage of podosomes and microtubules *J. Biol. Chem.* **285** 9506–15
[24] Wallace M R *et al* 1990 Type 1 neurofibromatosis gene: identification of a large transcript disrupted in three NF1 patients *Science* **249** 181–6
[25] Sharma R *et al* 2013 Hyperactive Ras/MAPK signaling is critical for tibial nonunion fracture in neurofibromin-deficient mice *Hum. Mol. Genet.* **22** 4818–28

J. Phys. D: Appl. Phys. 53 (2020) 014003

T Deguchi *et al*

[26] Illés T, Halmai V, de Jonge T and Dubousset J 2001 Decreased bone mineral density in neurofibromatosis-1 patients with spinal deformities *Osteoporos. Int.* **12** 823–7

[27] Brunetti-Pierri N *et al* 2008 Generalized metabolic bone disease in Neurofibromatosis type I *Mol. Genet. Metab.* **94** 105–11

[28] Alwan S, Tredwell S J and Friedman J M 2005 Is osseous dysplasia a primary feature of neurofibromatosis 1 (NF1)? *Clin. Genet.* **67** 378–90

[29] Stevenson D A *et al* 2011 Multiple increased osteoclast functions in individuals with neurofibromatosis type 1 *Am. J. Med. Genet.* A **155** 1050–9

[30] Heervä E *et al* 2010 Osteoclasts in neurofibromatosis type 1 display enhanced resorption capacity, aberrant morphology, and resistance to serum deprivation *Bone* **47** 583–90

[31] Yang F-C *et al* 2006 Hyperactivation of p21ras and PI3K cooperate to alter murine and human neurofibromatosis type 1–haploinsufficient osteoclast functions *J. Clin. Invest.* **116** 2880–91

[32] Pederson L, Ruan M, Westendorf J J, Khosla S and Oursler M J 2008 Regulation of bone formation by osteoclasts involves Wnt/BMP signaling and the chemokine sphingosine-1-phosphate *Proc. Natl Acad. Sci. USA* **105** 20764–9

[33] Koho S *et al* 2019 Fourier ring correlation simplifies image restoration in fluorescence microscopy *Nat. Commun.* **10** 3103

[34] Holtrop M E, Raisz L G and Simmons H A 1974 The effects of parathyroid hormone, colchicine and calcitonin on the ultrastructure and the activity of osteoclasts in organ culture *J. Cell Biol.* **60** 346–55

[35] Jurdic P, Saltel F, Chabadel A and Destaing O 2006 Podosome and sealing zone: specificity of the osteoclast model *Eur. J. Cell Biol.* **85** 195–202

[36] Destaing O, Saltel F, Géminard J-C, Jurdic P and Bard F 2003 Podosomes display actin turnover and dynamic self-organization in osteoclasts expressing actin-green fluorescent protein *Mol. Biol. Cell* **14** 407–16

[37] Saltel F, Chabadel A, Bonnelye E and Jurdic P 2008 Actin cytoskeletal organisation in osteoclasts: a model to decipher transmigration and matrix degradation *Eur. J. Cell Biol.* **87** 459–68

[38] Luxenburg C *et al* 2007 The architecture of the adhesive apparatus of cultured osteoclasts: from podosome formation to sealing zone assembly *PLoS One* **2** e179

[39] Meddens M B M *et al* 2016 Actomyosin-dependent dynamic spatial patterns of cytoskeletal components drive mesoscale podosome organization *Nat. Commun.* **7** 13127

[40] Saltel F, Destaing O, Bard F, Eichert D and Jurdic P 2004 Apatite-mediated actin dynamics in resorbing osteoclasts *Mol. Biol. Cell* **15** 5231–41

[41] Søe K and Delaissé J-M 2017 Time-lapse reveals that osteoclasts can move across the bone surface while resorbing *J. Cell Sci.* **130** 2026–35

[42] Wen P J *et al* 2016 Actin dynamics provides membrane tension to merge fusing vesicles into the plasma membrane *Nat. Commun.* **7** 12604

[43] Fritzsche M *et al* 2017 Self-organizing actin patterns shape membrane architecture but not cell mechanics *Nat. Commun.* **8** 14347

[44] Miklavc P *et al* 2012 Actin coating and compression of fused secretory vesicles are essential for surfactant secretion—a role for Rho, formins and myosin II *J. Cell Sci.* **125** 2765–74

[45] Milberg O *et al* 2017 Concerted actions of distinct nonmuscle myosin II isoforms drive intracellular membrane remodeling in live animals *J. Cell Biol.* **216** 1925–36

[46] Lee B 2018 Myosins in osteoclast formation and function *Biomolecules* **8** 157

[47] Ochoa G C *et al* 2000 A functional link between dynamin and the actin cytoskeleton at podosomes *J. Cell Biol.* **150** 377–89

[48] Bruzzaniti A *et al* 2005 Dynamin forms a Src Kinase–sensitive complex with Cbl and regulates podosomes and osteoclast activity *Mol. Biol. Cell* **16** 3301–13

[49] Bamburg J R and Bernstein B W 2010 Roles of ADF/cofilin in actin polymerization and beyond *F1000 Biol. Rep.* **2** 62

[50] Wiggan O, Shaw A E, DeLuca J G and Bamburg J R 2012 ADF/Cofilin regulates actomyosin assembly through competitive inhibition of myosin II binding to F-actin *Dev. Cell* **22** 530–43

[51] Blangy A, Touaitahuata H, Cres G and Pawlak G 2007 Cofilin activation during podosome belt formation in osteoclasts *PLOS One* **7** e45909

[52] Ozawa T *et al* 2005 The neurofibromatosis type 1 gene product neurofibromin enhances cell motility by regulating actin filament dynamics via the Rho-ROCK-LIMK2-Cofilin pathway *J. Biol. Chem.* **280** 39524–33

[53] Starinsky-Elbaz S, Faigenbloom L, Friedman E, Stein R and Kloog Y 2009 The pre-GAP-related domain of neurofibromin regulates cell migration through the LIM kinase/cofilin pathway *Mol. Cell. Neurosci.* **42** 278–87